International Journal of Fatigue 201 (2025) 109165

Contents lists available at ScienceDirect

International Journal of Fatigue

journal homepage: www.elsevier.com/locate/ijfatigue

Fatigue crack propagation in 15-5PH/316L bi-material steels fabricated by laser powder bed fusion

Anqi Liang [a], Songsong Lu [b], Mitchell Leering [c], Bilal Ahmed [c], Michael E. Fitzpatrick [c], Philippa A.S. Reed [a], Tomas Polcar [a], Andrew R. Hamilton [a,*]

[a] Engineering and Physical Sciences, University of Southampton, Southampton, United Kingdom
[b] Institute of Solid Mechanics, Beihang University, Beijing, China
[c] Engineering, Environment and Computing, Coventry University, Coventry, United Kingdom

ARTICLE INFO

Keywords:
Multi-material laser powder bed fusion
316L stainless steel
15-5PH stainless steel
Fatigue crack propagation
Residual stress

ABSTRACT

Multi-material laser powder bed fusion (MM-LPBF) offers the possibility of components with material and compositional complexity, as well as the geometric complexity for which additive manufacturing is known. LPBF materials are susceptible to fatigue failures due to stress concentrating roughness and porosity defects. Understanding fatigue failure processes is therefore important to enable adoption of multi-material parts, and suitable combinations of materials may offer a strategy to enhance fatigue performance by resisting crack propagation. This study focused on fatigue crack propagation in 316L/15-5 precipitation hardened (PH) bi-material stainless steels (SS), and the effect of residual stress distribution and yield stress gradient on fatigue crack propagation through the interface. The expected yield stress gradient effect in bi-materials (soft to hard interface) was simulated using FE models, showing a slight shielding effect with a drop in *J*-integral value. Contour cutting measurements detected a residual stress distribution near the bi-material interface that was tensile in 316L layer and compressive in 15-5PH layer. Fatigue crack propagation rates in bi-materials deviated from those in the corresponding single-material specimens. A relatively small shielding effect due to the yield stress gradient was detected within a short distance of the crack tip from the interface. However, the effects of residual stress were more pronounced and inhibited the crack growth rate by up to 77.8 % in regions of 15-5PH SS under residual compression, which suggesting that MM-LPBF parts can be designed such that the compressive residual stress is positioned to intercept and suppress propagating cracks to improve damage tolerance.

1. Introduction

Many engineering applications such as light water reactors [1] and engine blades [2] benefit from or require changes in material composition at different locations of a part or structure. Multi-material additive manufacturing (MMAM) techniques enable complex shapes to be produced using layer-wise deposition techniques and with control over the composition of material deposited in specific locations [3,4]. MMAM has enabled microscale compositional heterogeneity for producing microstructured composites with improved toughness [5], as well as integrally manufactured joints that remove the need for separate joining processes after shaping [6]. Multi-material laser powder bed fusion (MM-LPBF) AM enables these possibilities to be realised using engineering grade metal alloys and with the potential for small-scale geometric features and compositional variation, relative to other metal MMAM techniques such as direct energy deposition, due to the smaller laser-melt processing zone and layer heights of LPBF.

A common microstructural feature of LPBF metals are pores that occur as defects during processing [7]. Pores and other LPBF defects can act as stress concentrations that initiate damage, making LPBF materials generally susceptible to cracking and fatigue failures. Pores can also influence fatigue crack propagation by providing weaker pathways for rapid propagation, or causing crack path deviation [8,9], although the absence of these effects has been noted for LPBF processed 316L stainless steel with relatively high ductility and densification [10]. Cracks that initiate in one material of a multiple-material (MM) part might propagate through the interface and into the other and so the factors that affect interfacial crack propagation are important for understanding the damage tolerance and assessing lifetimes. The effect of a plasticity mismatch on cracks propagating perpendicular to the interface in a bi-

* Corresponding author.
E-mail address: a.r.hamilton@soton.ac.uk (A.R. Hamilton).

https://doi.org/10.1016/j.ijfatigue.2025.109165
Received 26 March 2025; Received in revised form 4 July 2025; Accepted 7 July 2025
Available online 7 July 2025

Table 1
Supplier specified chemical composition (wt%) of 316L SS and 15-5PH SS.

Element	Fe	C	Cr	Ni	Mo	Cu	Mn	Si	P	Nb	0	S	N
316L SS	Bal.	0.03	16–18	10–14	2–3	/	2	0.75	0.045	/	/	0.03	0.1
15-5PH SS	Bal.	0.04	14.6	4.5	/	4	0.3	0.7	0.03	0.4	0.03	0.03	0.1

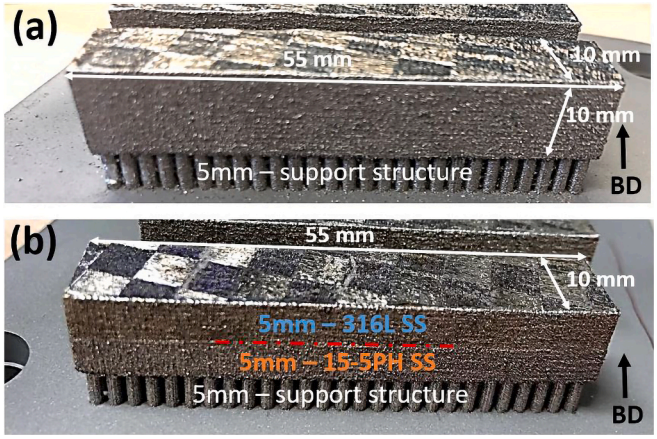

Fig. 1. Structure and geometry of fatigue test specimens for (a) 316L SS and 15-5PH SS single materials and (b) 316L SS/15-5PH SS bi-material bend-bar specimens.

material system has been analysed using analytical models [11,12] and investigated experimentally [13–15]. In analytical methods, the *J*-integral has been used as an indicator of the local crack driving force around the crack tips, and to predict crack growth rates. In regions far from a material interface, the near-tip *J*-integral (J_{tip}) is stable and equal to the applied far-field *J*-integral (J_{appl}). However, in a near-interface region, a crack that approaches an interface from a plastically weaker to a stronger material, the near-tip crack driving force is reduced ($J_{tip} < J_{appl}$) resulting in shielding of the crack tip and diminished crack growth rate in the vicinity of the interface. This concept is known as the yield stress gradient effect, and the opposite occurs (anti-shielding and enhanced crack growth rate) when a crack propagates from a stronger to weaker material. These shielding/anti-shielding effects can be enlarged by larger yield strength (YS) ratio between the interface materials [11,16]. The yield stress gradient effect has been further confirmed by experimental investigations. A reduction of crack propagation rate caused by crack tip bifurcation was observed by Pippan, R. et al. [17] when a crack grew towards a soft-to-hard interface of ARMCO iron/SAE 4340 steel (with a YS ratio of 3.8) produced by roll bonding. Fatigue crack propagation through the interface of 1Cr18Ni9Ti SS and 20G mild steel joined by explosive cladding (with a YS ratio of 1.7) exhibited shielding when the crack tip was 3 mm from the soft-to-hard interface and crack growth rate reached a minimum value at the interface. An anti-shielding effect was observed when the crack tip approached a hard-to-soft interface due to the fine-grained interfacial region caused by explosion cladding [13]. Crack shielding was also studied within laminated AA5005/AA2024 (with a YS ratio of 1.5) aluminium composite and AA5005 aluminium/DC1 steel composite (with a YS ratio of 2.7) joined by roll bonding. The variations of both Young's Modulus and YS between Al and Fe alloys made the steel layer a more effective barrier against crack propagation, resulting in a pronounced crack deviation at the soft-to-hard interface in AA5005/DC1 composite at both low and high stress amplitudes. However, in AA5005/AA2024 composite where only different YS exist, an effect of crack growth shielding was only observed at a high stress amplitude [18].

MM-LPBF has been used to process a range of metal and alloy combinations, including Fe/Cu alloys [3], Fe/Ni alloys [14], Fe/Al alloys [19], and Fe/Fe alloys [4]. Composition and hardness variations of MM-LPBF components have been widely reported, however, few studies have investigated fatigue crack growth behaviour near multimaterial interfaces. Santos, L. M. et al. studied fatigue crack propagation along interfaces of bi-materials consisting of LPBF maraging steel that was conventionally joined to H13 steel, 420 stainless steel and CK45E steel substrates [20]. In all material combinations, cracks initiated and grew on the LPBF side near and parallel to the interface, and the substrate steels had only negligible effects on crack growth rate. Fatigue crack propagation normal to the planar interfaces of MM-LPBF IN718 nickel superalloy and 316L SS was carried out by Duval-Chaneac, M. S. et al. [14]. A shielding effect was observed just before cracks crossed interfaces from soft 316L layers to hard IN718 layers (with a yield strength ratio of 1.15 between the two materials), and secondary cracks were observed within the 316L layer. Crack anti-shielding was also observed after propagation through interfaces from hard IN718 to soft 316L, which caused a threefold increase in the crack growth rate and occurred at a distance approximately equal to the plastic zone size from the interface.

Residual stress is another challenging outcome of laser-processed dissimilar joint alloys that occurs due to the different thermal expansion coefficients of dissimilar materials [21,22]. In a traditional single material LPBF process, residual stresses develop during the localised melting and solidification, which can be explained by the temperature gradient mechanism (TGM) model and the cool-down phase model [23,24]. The magnitude of residual stress depends on the material properties, part dimensions, base plate dimensions, and processing parameters [25]. However, in MM-LPBF components, the residual stress distribution is a superposition of solidification-induced residual stress from layer by layer solidification and a local residual stress near the MM interface due to the material property mismatch. Residual stresses have been investigated in MM-LPBF 316L SS/C52400 copper bi-materials and reportedly resulted in micro-cracks at the interface region that significantly influenced the bonding quality and tensile strength [26]. However, the effect of residual stress on fatigue crack propagation within LPBF bi-material components was not investigated.

This study focuses on MM-LPBF processing of two different grades of stainless steel: Lower strength high-ductility grade 316L SS (YS of 540 MPa and hardness of 228 HV) and higher strength lower ductility 15-5PH SS (YS of 843 MPa and hardness 373 HV) [27]. The interfacial microstructure resulting from MM-LPBF of 316L and 15-5PH SS has been reported to achieve a defect-free interfacial bond, and a YS ratio of 1.56 that is promising for crack shielding based on prior studies. Finite element (FE) models are implemented to estimate the magnitude of crack-tip shielding/anti-shielding. Single- and bi-material bend bars are manufactured and subjected to cyclic three-point bending to establish Paris-law crack growth rate behaviour for single materials and to assess the behaviour of fatigue crack growth at MM interfaces. The residual stress distribution along the cross-sectional plane of the crack path is measured to assess the possible impact of residual tension and compression on crack growth. Fracture surfaces are also observed to determine potential mechanisms affecting crack propagation. The results are useful for developing and evaluating MM LPBF microstructures as a strategy for producing parts with enhanced damage tolerance and extended fatigue lifetimes.

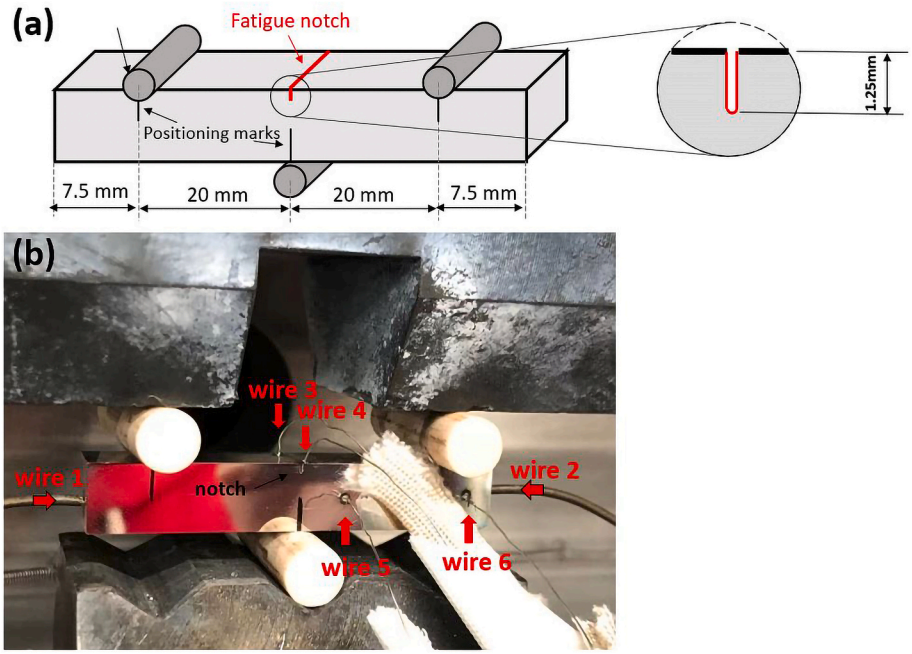

Fig. 2. (a) Schematic of three-point bending fatigue test set-up, and (b) photograph of test set-up connected with direct current potential drop recording device.

2. Materials and methods

2.1. Processing of single-/bi-material fatigue specimens

Gas atomized 316L SS and 15-5PH SS powders were supplied by Carpenter (USA) as CT PowderRange 316L and CT PowderRange 155F. The particles are nearly spherical with a specified size range of 15–45 μm. The chemical compositions of the powders specified by the manufacturer are listed in Table 1. Fatigue bend-bar specimens with total dimensions of 10 mm x 10 mm x 55 mm were manufactured using a Wuhan Huake 3D HK PM250 machine with a laser spot size of 0.15 mm and under an argon gas protective atmosphere. Single-material specimens of 316L SS and 15-5PH SS (Fig. 1(a)) and bi-material specimens with 316L SS as the top half layer (5 mm thick) and 15-5PH SS as the bottom half layer (5 mm thick, as in Fig. 1(b)) were all fabricated with manufacturer-suggested process parameters for SS: Laser power of 300 W, scanning speed of 900 mm/s, hatch spacing of 0.08 mm, and layer thickness of 0.03 mm. All specimens were built on cylindrical support structures (5 mm height, 1.5 mm outer diameter with 0.3 mm thickness) for convenient removal from the 316L SS baseplate. An island scanning strategy was used with a size of 5 mm. The scanning directions changed by 90 degrees in adjacent islands and the position of each island was randomised in each layer such that the boundaries did not overlap and such that the scanning direction was rotated 90 degrees between subsequent layers over portions of each island. These were the same processing conditions and equipment used to produce single-material and bi-material specimens of 316L and 15-5PH SS for microstructural characterisation previously reported by Liang, et al. [27].

2.2. Fatigue crack propagation tests

2.2.1. Fatigue test setup

Fatigue crack propagation tests were carried out under three-point bending Fig. 2(a), using an Instron 8502 servo-hydraulic machine, with sinusoidal loading at a stress ratio $R = 0.1$, and a cyclic frequency $f = 10$ Hz. The top surface of the specimens was ground using 120, 800, and 1200 grits abrasive papers and polished using 6 μm and 1 μm diamond paste to obtain a mirror-like surface finish. A wire-cut notch of 1.25 mm depth was made in the centre of the top surface. Crack length, a, was monitored by direct current potential drop (DCPD) method. The fatigue test set up connected with DCPD recording device is shown in Fig. 2(b). Wire 1 and 2 were welded onto far the left and right ends to provide a constant, direct electrical current passing through the sample. Wires 3 and 4 were welded on the top surface near to each side of the initial notch to measure the electrical potential fluctuations (E_{34}) due to the increase in resistivity with crack growth. The baseline potential of the current flow in the specimen was measured on the lateral side (away from the central notch) using wires 5 and 6 (E_{56}). The fatigue crack growth rates da/dN were then derived from the normalised electrical potential variation (E_{34}/E_{56}) versus time curve, translated to an empirically determined crack length (a) versus number of load cycles (N) [14], and da/dN was determined by the secant method. Crack profiles were observed using an Olympus BX41M-LED optical microscope (OM). Fracture surface analysis was carried out using a *Vision Engineering*@ EVO CAM II Microscope and JSM-7200F Field Emission Scanning Electron Microscope (SEM).

2.2.2. Fatigue test of single materials

Paris law behaviour of single material 316L SS and single material 15-5PH SS, used to establish base line crack growth behaviour, were evaluated under a load ratio of $R = \sigma_{min}/\sigma_{max} = 0.1$, with constant load and therefore increasing ΔK with crack growth, according to BS ISO 12108:2018 [28]. The stress intensity factor K was calculated as $K = Y \bullet \sigma \bullet \sqrt{\pi \bullet a}$, where Y is a dimensionless geometric factor (defined in Eq. (1), σ is the applied stress, a is the crack length, and W is the specimen width [29,30].

$$Y = \frac{6\left(\frac{a}{W}\right)^{1/2}\left[1.99 - \left(\frac{a}{W}\right)\left(1 - \frac{a}{W}\right)\left(2.15 - 3.93\left(\frac{a}{W}\right) + 2.7\left(\frac{a}{W}\right)^2\right]\right.}{\left(1 + 2\frac{a}{W}\right)\left(1 - \frac{a}{W}\right)^{3/2}} \quad (1)$$

Before the tests, pre-cracking was carried out by load shedding from an initial ΔK (13 MPa$\sqrt{m}$ for 316L SS and 12 MPa$\sqrt{m}$ for 15-5PH SS). After the pre-cracks grew through 4 monotonic plastic zone sizes, the load was successively stepped down by 10 % increments to initial ΔK of 10.77 MPa$\sqrt{m}$ for 316L and 7.49 MPa$\sqrt{m}$ for 15-5PH SS and loading was maintained constant so that ΔK increased with crack growth until failure. The plastic zone sizes were estimated based on Irwin's model and

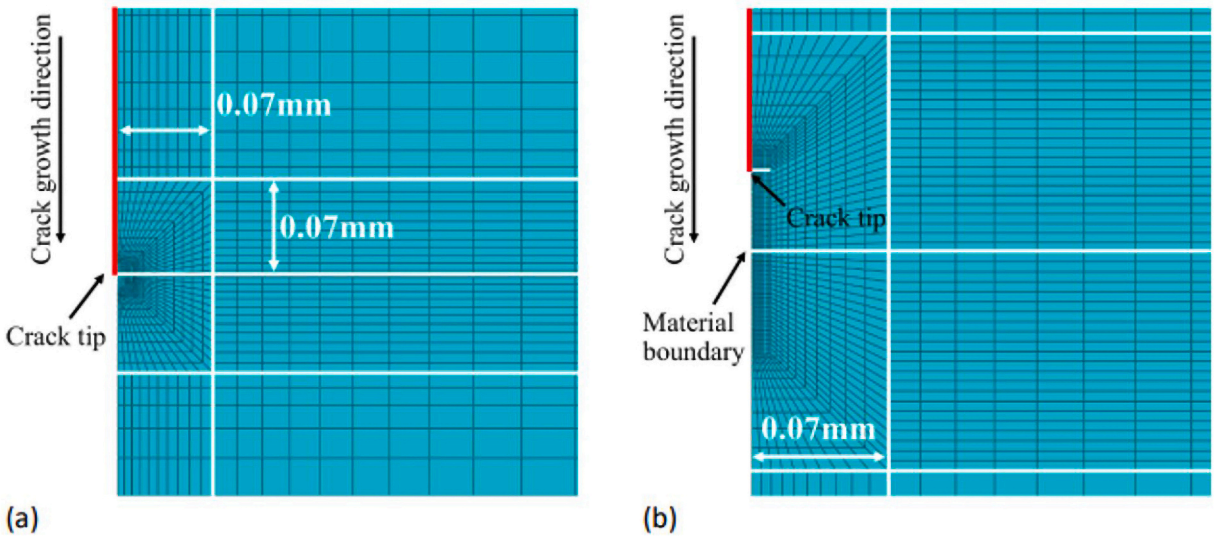

Fig. 3. Mesh around the crack tip when (a) the crack tip was far from the interface and (b) the crack tip was near to the interface. Reproduced with permission [34] © Elsevier. Reprinted by permission of the publisher via Copyright Clearance Center.

Table 2
Tensile test properties of 316L SS and 15-5PH SS [27].

	Ultimate tensile strength, *UTS* (MPa)	Yield strength, $YS_{0.2}$ (MPa)	Young's modulus, *E* (GPa)	Poisson's ratio, ν
316L SS	639.03 ± 1.2	540.6 ± 11.9	186.5 ± 4.1	0.25
15-5PH SS	1091.72 ± 17.6	843.9 ± 14.0	190.1 ± 7.1	0.27

assuming plane strain, with fracture toughness values of K_{IC} = 300 MPa$\sqrt{m}$ and 47 MPa$\sqrt{m}$ for 316L [31] and 15-5PH [32], respectively, and with yield strength values of σ_y = 540.6 MPa and 843.9 MPa for 316L and 15-5PH [27], respectively. To make a comparison of crack growth rate between two single materials, a single value of ΔK = 11 MPa$\sqrt{m}$ was selected from within the range of Paris law behaviour for both materials to perform constant-ΔK fatigue tests (R = 0.1) for each single material, which was achieved by altering the loading condition as the crack advanced to maintain ΔK within 10 % of the original value.

2.2.3. Fatigue tests of bi-materials

Two constant load range fatigue tests were performed for 316L SS/15-5PH SS bi-material components, one notched on the 316L SS side and one notched on the 15-5PH SS side. The testing procedure was similar to that for single materials described above. Pre-cracking was carried out from an initial ΔK of 13 MPa$\sqrt{m}$ until the crack grew through 4 monotonic plastic zone sizes. After pre-cracking, initial load amplitudes were selected for ΔK values of 10.77 MPa$\sqrt{m}$ (notched on the 316L side) and 8.12 MPa$\sqrt{m}$ (notched on the 15-5PH SS side), with R = 0.1 and load amplitudes constant and therefore ΔK increasing with crack growth until failure. In addition, a constant ΔK fatigue test (ΔK = 11 MPa$\sqrt{m}$, R = 0.1) was also performed on the 316L SS/15-5PH SS bi-material specimen that was notched on the 316L SS side.

2.3. Modelling of J-integral

To investigate the shielding/anti-shielding effect on the fatigue crack driving force due to the change in plastic properties in bi-material components, the *J*-integral of the crack tip field was computed for different crack lengths subjected to a given (constant) ΔK of 11 MPa$\sqrt{m}$. This was calculated using finite element (FE) models of bi-material bend-bar specimens with an interface in the middle of the height and with a notch on the 316L SS side. 2D FE models for simplified bi-materials with the dimensions shown in Fig. 2(a) and subjected to three-point bending conditions were implemented in Abaqus (Dassault, v. 6.12). Symmetric boundary conditions were applied to the vertical central line of the bend-bar specimen. The linear plane strain element CPE4R, 4-node reduced integration bilinear plane strain quadrilateral element, was chosen. A structured meshing technique was applied, as shown in Fig. 3 near the crack tip, and similar to the mesh adopted and verified by Kolednik O. et al. [33]. When the tip was far from the bi-material interface, the size of the refined mesh boundary was 0.07 mm × 0.14 mm (Fig. 3 (a)). When the crack tip was near to the material interface (Fig. 3 (b)), the material interface was located at the centre of the refined mesh area and at least nine elements were present between the crack tip and the material interface [33].

The tensile stress–strain response of 316L SS and 15-5PH SS applied in this model as materials constitutive models were experimentally measured and are reported in Table 2 [27]. The *J*-integral was used to quantify the crack driving force based on linear elastic fracture mechanics (LEFM) assumptions of small-scale yielding conditions. It was calculated by the contour integral method using the fifth rectangle contour around the crack tip, which never interacts with the material interface, satisfying its path-independence requirements. A detailed description of the modelling method has been presented in a previous study by the authors [34].

2.4. Residual stress evaluation

Residual stresses within the single material 316L SS components and 316L SS/15-5PH SS bi-material components joined by LPBF were evaluated by two methods: Incremental centre hole drilling and the contour method.

Incremental hole drilling, which is based on measuring the elastic material relaxation by removing material through stepwise drilling, was carried out using a *Stresscraft Ltd*[@] orbital milling incremental hole drilling apparatus. Holes were drilled to a maximum depth of 1048 μm at about 20 mm from the right edge of the sample and along the centre line on the top and bottom surfaces of a bi-material bend-bar specimen. Schematics of hole drilling points are shown in Fig. 4. Drilling increments were defined as six steps of 16 μm each, five steps of 32 μm each, six steps of 64 μm each, and six steps of 128 μm each. The residual stress was then calculated using Stresscraft RS INT software which is

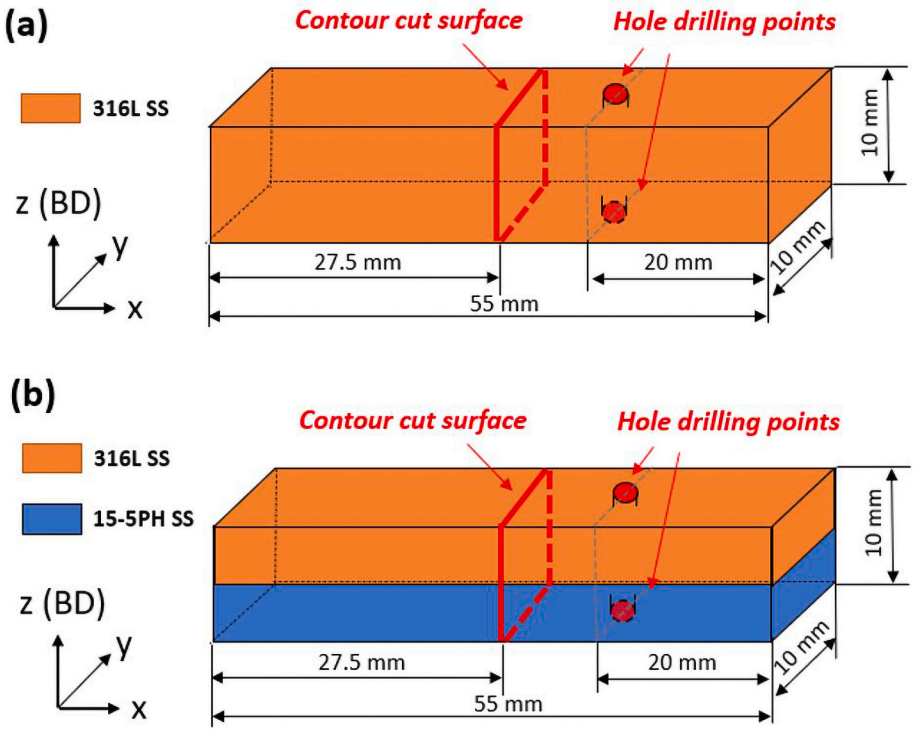

Fig. 4. Schematics of residual stress measurement by hole drilling method and contour cut method on (a) single material 316L SS, and (b) 316L SS/15-5PH SS bi-material.

based on the ASTM E837 integral method with a moving average smoothing technique applied to the strains [35]. All the measurements were conducted using Vishay Micro Measurement three-element gauge rosettes (EA-13-062RE-120).

Due to the measuring depth limit of the hole drilling method, the contour method was conducted on a cross-section located 27.5 mm along the longitudinal axis of bend-bar specimens (as shown in Fig. 4) to evaluate the residual stress distribution over the entire cross-sectioned surface (10 mm × 10 mm) of single material 316L SS and bi-material specimens. The specimens were cut by a Fanuc Robocut α-C600i wire electro-discharge machine with a 0.25-mm-diameter brass wire. The cutting speed through the sample was about 0.25 mm/min. The surface displacement profiles of cross-sectioned surfaces of specimens were captured with a Zeiss Contura g2 coordinate measuring machine (CMM). A 3-mm-diameter touch probe was used to detect displacement with a spacing of 0.1 mm between the individual measurement points. The displacement data was post-processed for data aligning, cleaning, flattening, and smoothing using Matlab. The data smoothing of all samples was performed using a cubic spline with knot spacing of 1.5 mm along the building (z, BD) and horizontal directions (y). An FE model of a cut half of the sample was built with 8-node brick element (C3D8R) in the software Abaqus (Dassault, v. 6.12) with a mesh size of 0.2 mm. The reverse of the measured and smoothed contour was applied as the displacement boundary condition. Constraints were applied to avoid rigid body motion. Finally, a linear elastic FE analysis with the material properties of 316L SS and 15-5PH SS (as shown in Table 2) was performed to compute the predicted residual stress distribution present in the samples before cutting.

3. Results and discussion

3.1. Residual stress distributions

A detailed assessment of the microstructure of single-material and bi-material specimens of 316L and 15-5PH SS was reported by Liang, et al. [27]. In bi-materials at locations far from the interface, elongated austenitic grains were reported within the 316L SS (average sizes of 107.9 μm) and finer martensitic lathes were reported in 15-5PH (average sizes of 5.9 μm). Near the interface, a refined region of 15-5PH with higher recrystallisation was observed with ~75 % reduced lathe size over a distance of about 120.7 μm below the interface. The interface itself was wavey due to the circular shape of the melt pools, and the interface position varied in the build direction by ~57.4 μm, about twice the size of the powder layer thickness used for LPBF processing (30 μm). The composition of the SS, as measured by energy-dispersive spectroscopy (EDS), transitioned over a shorter distance of about of 7 μm across the bi-material interface. Microscopic inspection at a selected cross-section revealed no apparent pores, cracks, or defects at the interface, and overall porosity < 0.1 % consistent with the porosities in the single materials. The average yield strength of single-material 15-5PH SS was reported as 843.0 MPa and an average strain to failure of 2.3 %. As expected, the yield strength of single-material 316L was lower (average of 540.6 MPa) and strain to failure higher (average value of 34.3 %). The residual stress distribution of single material 316L SS and bi-material 316L/15-5PH SS are displayed in Fig. 5. The results obtained from the hole drilling method are represented with orange points, showing the residual stress distribution along 1 mm from top and bottom surfaces in the building direction (BD). Both specimens showed similar residual stress distributions, with tensile residual stresses ranging from 200 MPa to 250 MPa close to the top and bottom surfaces that reduced farther from the surfaces. The residual stress distribution maps obtained from contour cut methods are also displayed in Fig. 5 as coloured contours, and the residual stress values along the vertical centreline of the 10 x 10 mm^2 cross-section surface are shown as blue data points. In Fig. 5(a) along the BD the residual stress map of single 316L SS appeared relatively steady with small tensile stresses below the top surface (~68 MPa) and above bottom surface (~133 MPa) and a broad region of mild compressive residual stress in the centre (~-57 MPa). This general distribution is consistent with the temperature gradient mechanism (TGM) model and cool-down phase model put forward by Mercelis, P. et al.

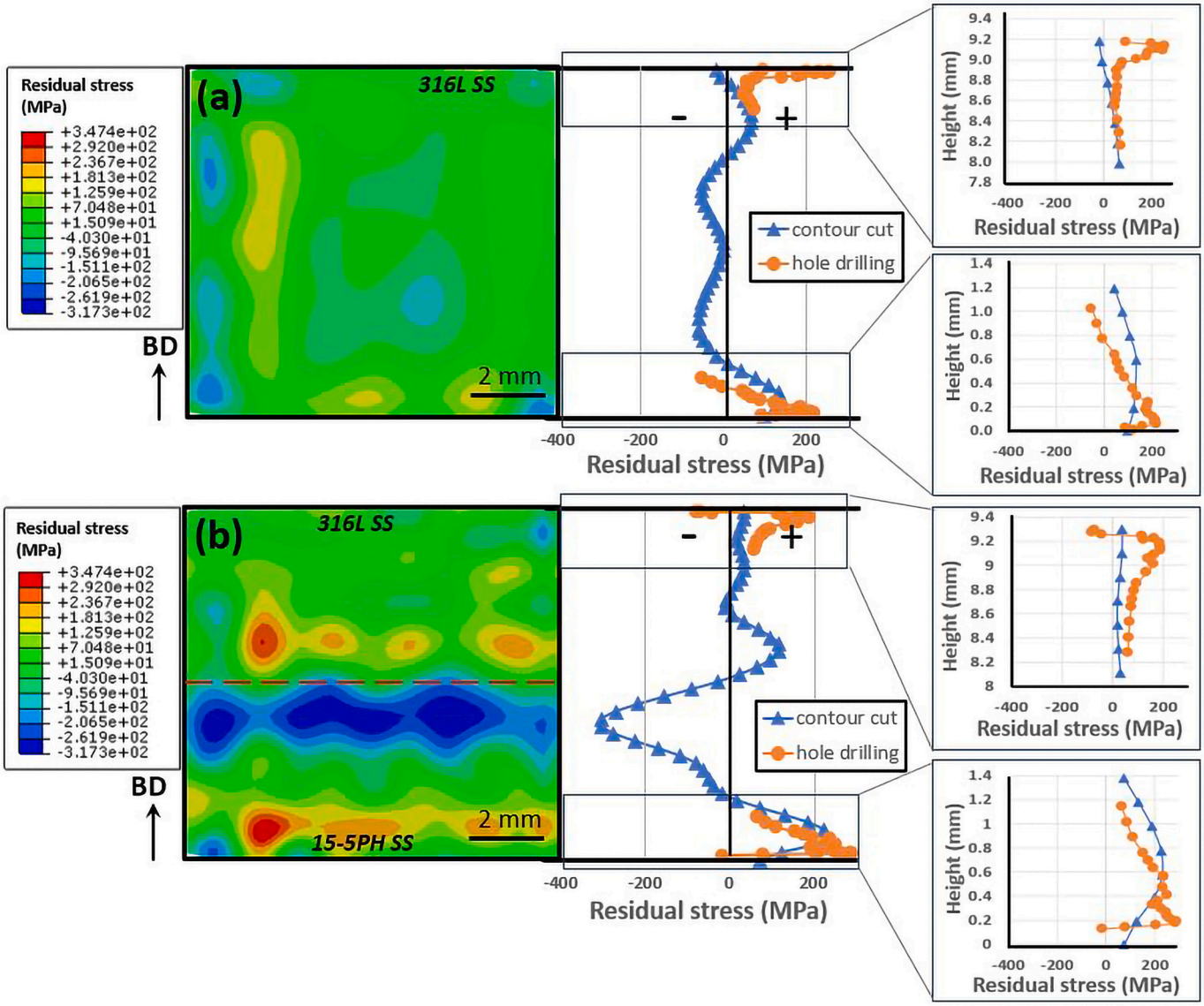

Fig. 5. Contour-cut residual stress maps and center line plot compared with hole drilling results for (a) single-material 316L SS and (b) 316L SS/15-5PH SS bi-material. Building direction, BD, is indicated by an arrow.

[25], which assumes that constrained expansion upon heating and constrained contraction upon cooling results in tensile residual stresses near the top of an LPBF part, balanced by residual compression in the layers below. When an LPBF part is removed from the base plate, residual stresses rebalance resulting in tension at the new free surface, compression internally, and tension at the top surface where processing ceased. Other experimental studies have also confirmed this expected distribution [36–38].

Similar to single material 316L SS, the residual stress in the bi-material specimen (Fig. 5(b)) was higher and tensile (~230 MPa) near the bottom surface, and smaller and tensile (~36 MPa) near the top surface. At the interface, a residual tensile stress of about 119 MPa was measured above the interface on the 316L SS side (top) and a larger residual compressive stress (~-303 MPa) was measured on the 15-5PH SS side (below), which can be attributed to the higher thermal expansion coefficient (CTE) of 316L SS (17.2×10^{-6} °C $^{-1}$) compared to 15-5PH SS (10.8×10^{-6} °C $^{-1}$). During the bi-material manufacturing process, 15-5PH SS was fabricated first. After finishing the last layer of 15-5PH SS, 316L SS powder was spread and laser processed on the previously solidified 15-5PH SS layer. The larger thermal expansion coefficient of 316L SS would have caused a larger differential expansion and contraction during heating and cooling compared to 15-5PH SS, resulting in higher residual stresses. A similar result was also reported in a dissimilar welded joint between SAF2205 duplex stainless steel and 304 austenitic stainless steel. A compressive residual stress was obtained in near-interface region of SAF2205 side, which has a lower thermal expansion coefficient compared to 304 SS [39]. Residual stresses obtained from the hole drilling method and contour cut method are largely comparable in the regions within 1 mm distance from top and bottom interfaces for both specimens. In both specimens, results of both methods in the bottom 1 mm region are consistent with similar trend and magnitude, which confirms the validity of results from both methods. In the top 1 mm region, hole drilling results show a tensile residual stress, which is as expected in the LPBF process explained by cool-down phase model, however the result from the contour cut method was a low residual tensile stress very close to 0 in both specimens. The difference might be attributed to: (1) the fact that the contour cut method is more likely to miss residual stresses near boundaries because the out-of-plane deformations (which are measured and used to calculate residual stress with this method) near the boundaries of the specimen are more likely to be affected by the free surfaces and the lower levels of control over the cross-sectional cutting; (2) the location

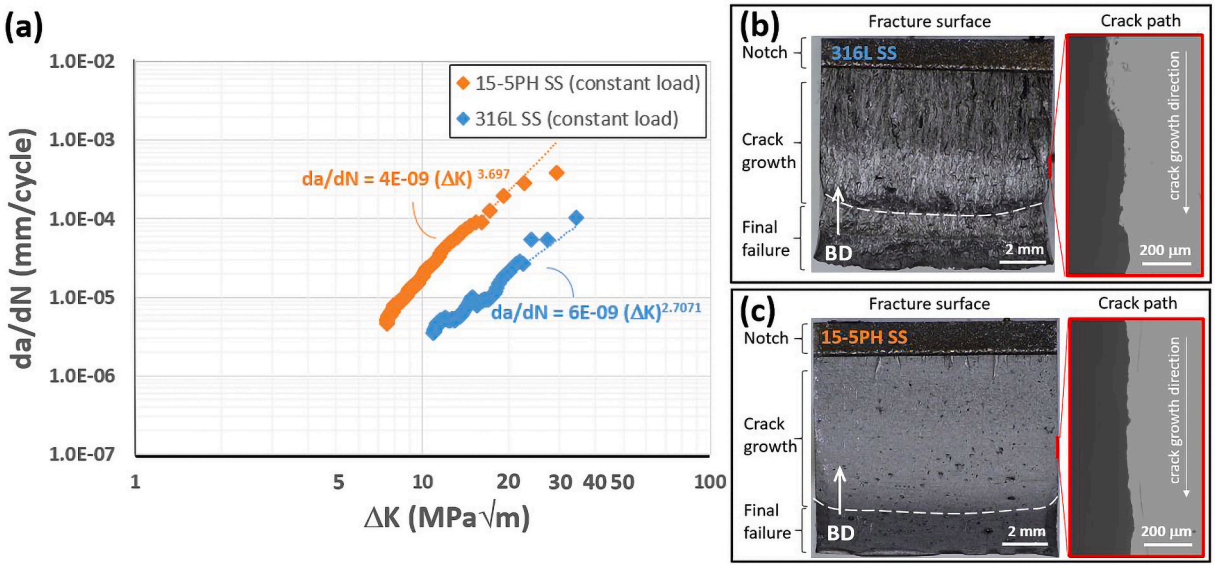

Fig. 6. (a) Crack growth rate, *da/dN*, versus stress intensity factor range, Δ*K*, at constant load (rising Δ*K*). Corresponding fracture surfaces with side views of the crack path (within a region of interest, marked red) for (b) single-material 316L SS and (c) single-material 15-5PH SS. Building direction, BD, and crack growth direction are indicated by arrows.

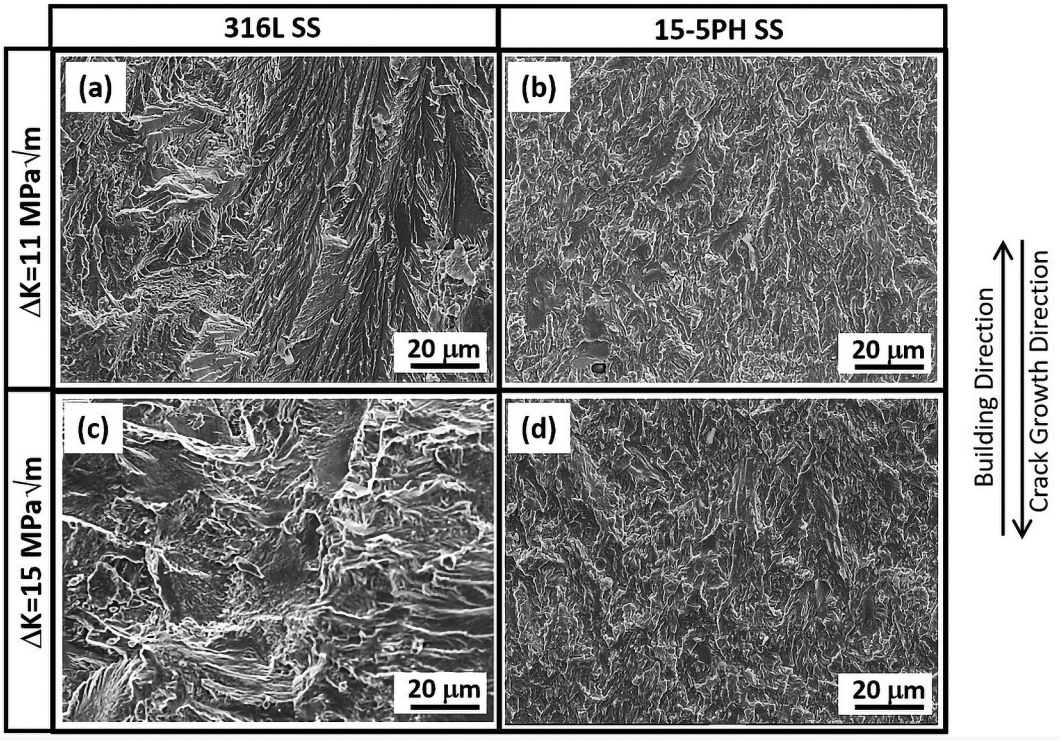

Fig. 7. SEM fractography for (a, c) single 316L SS and (b, d) single 15-5PH SS under constant load fatigue at locations corresponding to ΔK values of 11 MPa$\sqrt{m}$ (top) and 15 MPa$\sqrt{m}$ (bottom), respectively. Building direction and crack growth direction are indicated by arrows.

where hole drilling was carried out and the location where contour cut was taken would have been positioned differently within laser scan islands with varying scan directions, the details of which were not determined in this study; (3) after removal from the substrate the specimen surfaces were ground and polished, which is expected to induce small tensile residual stress on the surfaces that would superpose differently with residual stress from laser scanning within islands at different locations.

3.2. Fatigue crack propagation of single materials

3.2.1. Constant load testing

Fatigue crack propagation tests were performed under cyclic loading with a constant load (rising stress intensity factor range, Δ*K*, with increasing crack length, *a*) for single-material LPBF 316L SS and single-material LPBF 15-5PH SS to evaluate the crack propagation behaviour. The resulting crack growth rates, d*a*/d*N*, are shown as a function of rising Δ*K* in Fig. 6(a). Fracture surfaces are also shown along with a side

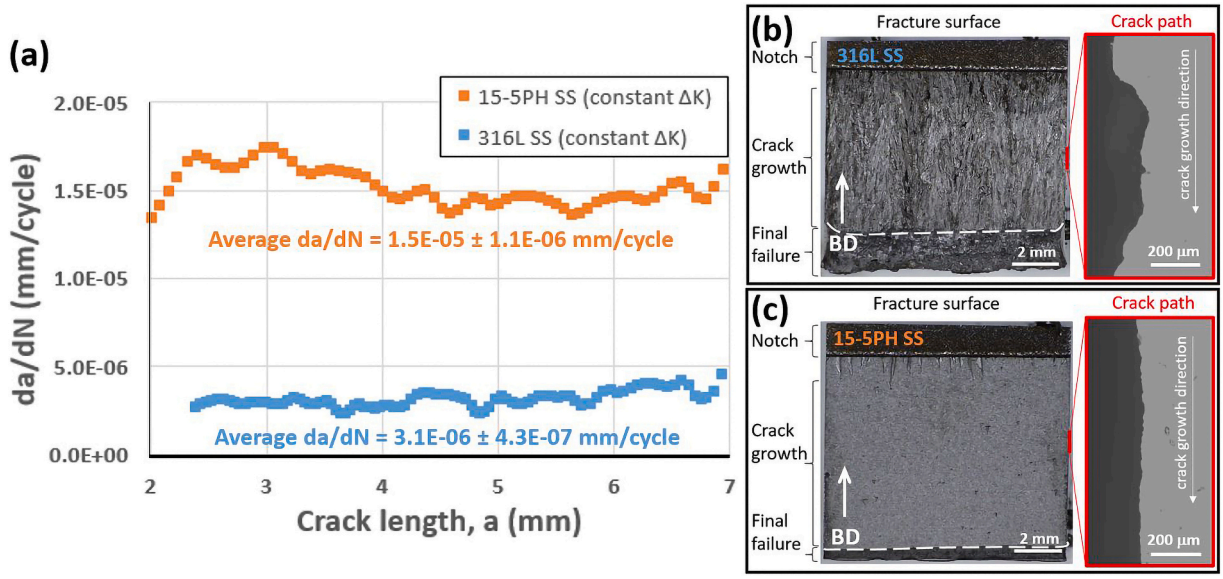

Fig. 8. (a) Crack growth rate, da/dN, versus crack length, a, under constant ΔK of 11 MPa$\sqrt{m}$ (decreased load with increased a). Corresponding fracture surfaces with side views of crack path (within a region of interest, marked red) for (b) single-material 316L SS and (c) single-material 15-5PH SS. Building direction, BD, and crack growth direction are indicated by arrows.

view of crack path in Fig. 6(b) and (c). The Paris Law behaviour of 316L SS (blue points) and 15-5PH SS (orange points) within the range of $\Delta K = 5 - 40$ MPa$\sqrt{m}$ is described by the following equations (2) and (3), obtained by power law curve fitting to the experimental data.

$$316\text{L SS}: \frac{da}{dN} = 6 \times 10^{-9} \Delta K^{2.7} \quad (2)$$

$$15-5\text{PH SS}: \frac{da}{dN} = 4 \times 10^{-9} \Delta K^{3.7} \quad (3)$$

The Paris Law behaviour of 316L SS is similar to other studies on crack growth of LPBF 316L SS: For compact tension (CT) specimens, da/dN = $2.12 \times 10^{-9} \Delta K^{3.37}$ [10] and da/dN = $1.6 \times 10^{-8} \Delta K^{2.64}$ [40] were reported for a crack growing parallel to the BD. The slight variations in Paris exponents can be attributed to different processing conditions (energy densities) and testing conditions (processing temperatures). Crack propagation data for LPBF 15-5PH SS could not be found for comparison. The Paris law plot indicates that with the same level of ΔK, a higher crack growth rate occurred in 15-5PH SS, which is expected for this martensitic steel with higher strength, lower ductility, and smaller grain size.

Comparing the fracture surfaces and side-view crack paths of both materials (Fig. 6(b) and (c)), 316L SS appeared rougher with a more tortuous crack path while 15-5PH SS was smoother with a flat and straight crack path. Some defects were observed in 15-5PH SS, with more large defects distributed at the bottom of the fracture surface, where ΔK was higher than the top. As reported by Liang, A. et al. [27], the distribution of defects in LPBF 15-5PH SS specimens with the same dimensions and processing conditions was uniform along the building direction. This suggests that the larger defects in Fig. 6(c) are not due to manufacturing, but because of the higher ΔK with more crack extension each cycle which is expected to cause a rougher fracture surface. More of these defects appear within the 15-5PH SS specimen than in 316L SS, which might contribute to the faster crack growth rate. Crack growth is regarded as a mutual competition between intrinsic microstructural damage mechanisms, which promote crack extension ahead of the tip, and extrinsic crack-tip shielding mechanisms, which act primarily behind the tip to retard crack growth [41]. From tensile tests, the elongation to failure of 316L SS is 34 % and is only 2.3 % for 15-5PH SS [27]. The more ductile behaviour of 316L SS contributes to better damage-tolerance compared to 15-5PH SS. Grain size is another significant factor that influences fatigue crack growth. A martensitic microstructure with an average grain size of 5.9 µm was observed for 15-5PH SS, and 316L SS has an austenitic microstructure with an average grain size of 107.9 µm [27]. Larger grains are associated with a more deflected crack path (evidenced by a rougher fracture surface). This leads to opening of the crack when asperities contact prematurely on unloading, and therefore shielding via closure and slower crack propagation in 316L SS [42].

Fig. 7 shows SEM images of fracture surfaces at locations corresponding to ΔK values of 11 and 15 MPa$\sqrt{m}$ for 316L SS and 15-5PH SS, respectively. In 316L SS (Fig. 7(a) and (c)), large vertically elongated grains along the BD are present, which is typical for LPBF processed 316L SS. Tearing marks, with elongated features between the adjacent planes of different grains, present as ridge-like features. Fatigue striations are present between adjacent ridges, indicating the local crack growth direction, and revealing small deflections from the main cracks. Fracture surfaces of 15-5PH SS at both ΔK levels showed transgranular cleavage features with the crack propagation through the crystallographic planes. The smooth fracture surface is consistent with the fine grain size.

3.2.2. *Constant ΔK testing*

To further examine and compare the fatigue crack propagation behaviour between 316L SS and 15-5PH SS, fatigue crack propagation tests were performed at constant stress intensity factor range of $\Delta K = 11$ MPa$\sqrt{m}$ for both steels. The crack growth rate (da/dN) versus the crack length (a) plots for 316L SS (blue) and 15-5PH SS (orange) are shown in Fig. 8(a) with the average crack growth rates with standard deviations displayed for each. With increasing crack length, both materials exhibited stable crack growth rates with only slight fluctuations (standard deviations an order of magnitude below the averages) and which correspond closely with the crack growth rates obtained from the constant load fatigue tests (Fig. 6) at the same $\Delta K = 11$ MPa$\sqrt{m}$.

Fig. 8(b) and (c) show fracture surfaces are similar to those obtained from constant load tests, i.e., rougher and more tortuous crack path for 316L SS and smoother and flatter crack path for 15-5PH SS. However, the fracture surface of 15-5PH SS with constant ΔK (Fig. 8(c)) revealed no large defects, and the distribution of defects is more uniform from the top to the bottom at different crack lengths, again suggesting enlarging

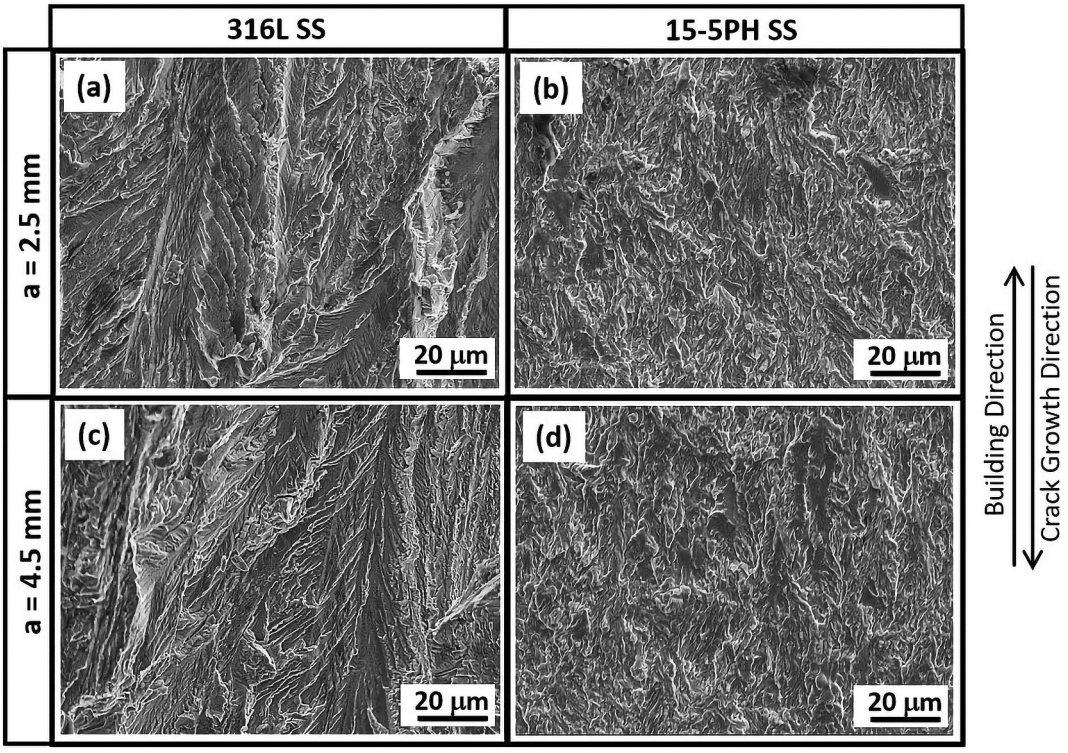

Fig. 9. SEM fractography for (a, c) single-material 316L SS and (b, d) single-material 15-5PH SS under constant-ΔK (11 MPa$\sqrt{m}$) testing at different locations with crack length of 2.5 mm (top) and 4.5 mm (bottom), respectively. Building direction and crack growth direction are indicated by arrows.

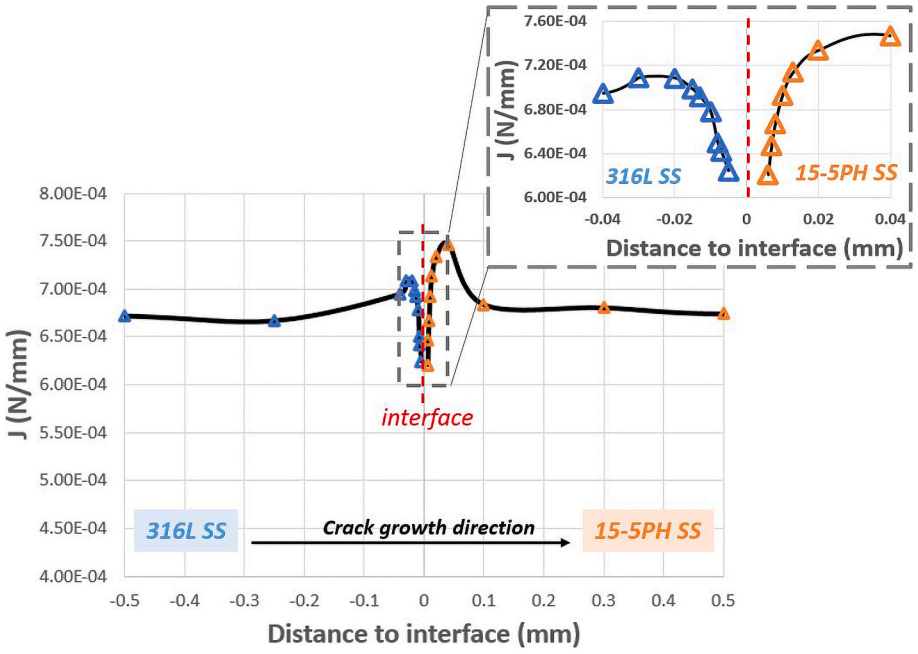

Fig. 10. Values of J-integral at different distances from the crack tip to a bi-material interface as the crack extends from 316L SS to 15-5PH SS at a constant ΔK of 11 MPa$\sqrt{m}$.

defects at higher ΔK (Fig. 6(c)). These may have been caused by small pores formed during LPBF processing being opened and elongated by rapid crack extension at high ΔK.

Fig. 9 shows SEM images of the fracture surfaces at different locations, corresponding to crack lengths of 2.5 mm (Fig. 9(a) and (b)) and 4.5 mm (Fig. 9(c) and (d)) for both materials. At longer crack lengths, there is no difference in fracture surface features due to the constant ΔK and thus uniform crack tip driving force throughout the test. Comparing Fig. 9(a) and (c) to the SEM images displayed in first row of Fig. 6(a), the fracture surfaces of both 316L and 15-5PH SS are similar at the same ΔK level in constant load and constant ΔK tests.

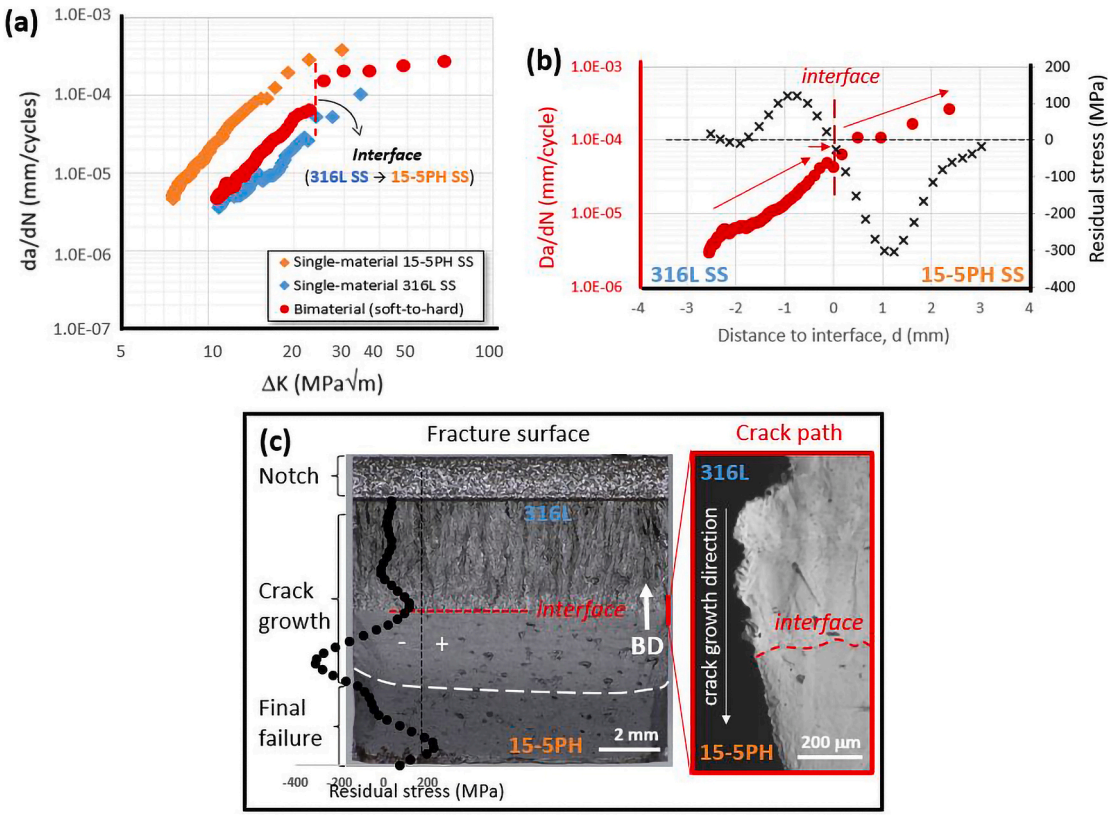

Fig. 11. (a) Crack growth rate, da/dN, versus stress intensity factor range, ΔK, (b) da/dN (red circles) and residual stress (black crosses) from contour cut method versus distance from crack tip to interface, d, and (c) full fracture surface with side views of the crack path (within a region of interest, marked red) for a bi-material with crack growing from 316L SS to 15-5PH SS under constant load. Building direction, BD, and crack growth direction are indicated by arrows.

3.3. Simulation of yield stress gradient effect for 316L SS/15-5PH SS bi-material

The J-integral is related to the stress intensity factor, K, based on the Rice-Irwin relation, and can be used to characterize the crack tip driving force taking into account effects of plasticity in elastic–plastic fracture. To explore the effect of plasticity mismatch on crack propagation across bi-material interfaces, the J-integral was calculated using an FEA Model of a 316L SS/15-5PH SS bi-material specimen with a crack growing from the 316L SS side towards the interface under constant ΔK. With a crack growing from a weaker to stronger material, suppression of crack growth and the corresponding J-integral is expected. As suggested by Irwin, the radius of the monotonic plastic zone ahead of the crack tip, r_p, was estimated for a plane strain condition using Equ. (4) [43]:

$$r_{pl} = \left(\frac{1}{6\pi}\right) \times \left(\frac{K_{max}}{\sigma_y}\right)^2 \propto \left(\frac{K}{\sigma_y}\right)^2 \quad (4)$$

At a constant ΔK of 11 MPa$\sqrt{\text{m}}$ with a stress ratio of 0.1, the plastic zone size ahead of the crack tip was estimated to be 0.027 mm within the 316L SS layer and 0.011 mm within the 15-5PH SS layer. This estimate assumes an isotropic yield strength when, in fact, variation is expected due to the elongated columnar grains and crystallographic texture produced by LPBF, especially for 316L SS [27].

Fig. 10 shows the J-integral variations with different distances from the crack tip to the interface. A crack was firstly located 3.5 mm ahead of interface, and J-integral values were calculated at every 0.5 mm of crack extension from 316L SS to 15-5PHSS until reaching a distance of 1.5 mm after the interface. At the near-interface region (within ± 0.5 mm distance to interface), the crack extension resolution was gradually reduced from 0.2 mm, 0.1 mm, 0.01 mm to 0.001 mm as the crack approached the interface. When the crack tip was far from the interface, the calculated J-integral values were approximately constant (around 6.91 × 10^{-4} N/mm) due to the constant ΔK. When the crack tip gradually approached the interface from the 316L SS side, the J-integral slightly increased by 2.6 % and reached a maximum of 7.09 × 10^{-4} N/mm at 0.03 mm ahead of the interface (which is similar to the r_p = 0.027 mm for 316L SS), followed by a drop to minimum of 6.24 × 10^{-4} N/mm (a decrease by 9.6 % compared to far-interface 316L SS layer) when closest to the interface (distance of 0.005 mm). When approaching a stronger material, an incremental crack extension produced a change in the total plastic strain energy of the body and therefore reduced the near-tip crack driving force represented by the J-integral values, resulting in shielding of the crack tip [11]. After the crack penetrated the 15-5PH SS side of the interface, the J-integral significantly increased to a maximum 7.47 × 10^{-4} N/mm (8.1 % increase compared to far-interface region) at 0.04 mm from the interface. As the crack continued to grow farther away from the interface, the J-integral values dropped to the similar level to that in 316L SS.

3.4. Fatigue crack propagation of 316L/15-5PH bi-materials at constant load

Two constant load tests were carried out for bi-materials: soft-to-hard (crack propagated through the interface from 316L SS to 15-5PH SS) and hard-to soft case (crack propagated through the interface from 15-5PH SS to 316L SS). In the following sub-sections, the crack propagation performances in both cases are discussed separately.

3.4.1. Crack propagation from 316L to 15-5PH SS (soft-to-hard)

For the soft-to-hard case, the crack growth rate (da/dN) versus stress intensity factor range (ΔK) relationship (red markers) is shown in Fig. 11 (a), with comparisons to the baseline performances of single material 316L SS (blue markers) and 15-5PH SS (orange markers). The interface

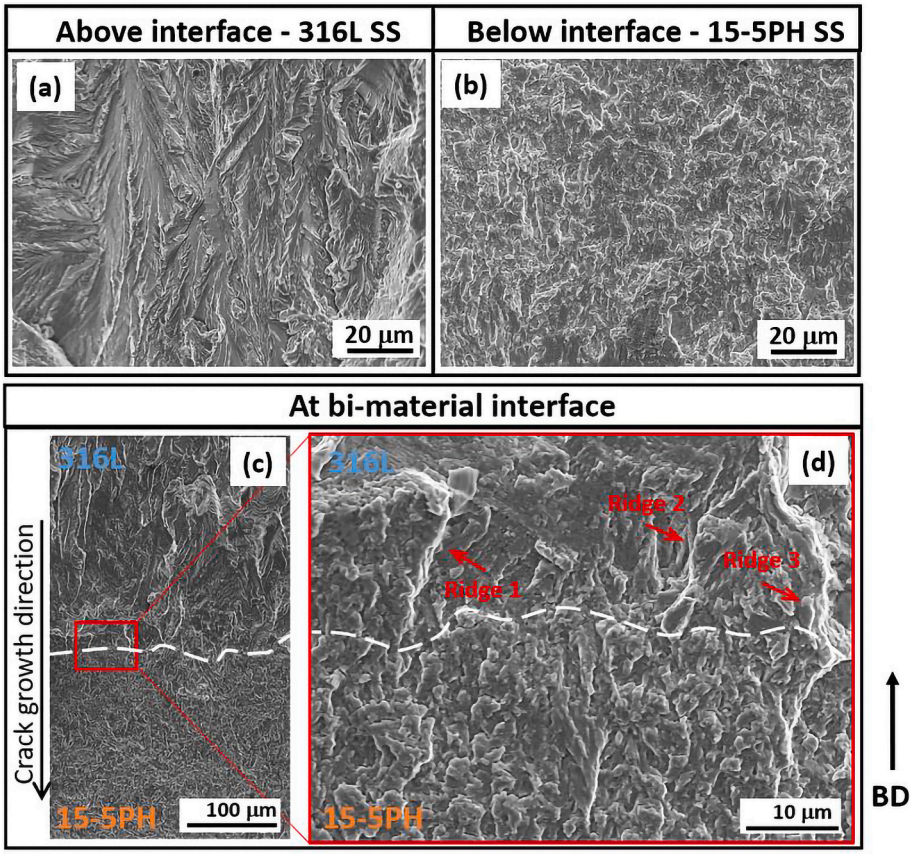

Fig. 12. SEM fractography at different locations within a bi-material specimen after fatigue crack growth from 316L SS to 15-5PH SS at constant load: (a) 316L SS layer above the interface, (b) 15-5PH SS layer below the interface, and (c, d) the interfacial region (with 316L above and 15-5PH below) at low and high magnifications. Building direction, BD, and crack growth direction are indicated by arrows.

location is marked out by a red dashed line. The da/dN (red circles) and residual stress measured by contour cut method (black crosses) versus distance of crack tip to interface, d, are plotted in Fig. 11(b). At the far-interface region (farther than 1.28 mm ahead of interface, $d < -1.28$ mm), the crack growth rate increased steadily due to the increasing ΔK, which is similar to the trend and values of da/dN vs. ΔK observed for single material 316L SS (blue markers). From 1.28 mm ahead of interface, da/dN appeared higher than the single material 316L SS, the higher crack growth rate might be caused by the higher tensile residual stress (up to 119 MPa) in the bi-material specimen from d = -2 mm to d = 0 mm (Fig. 11(b)). When the crack propagated to 0.3 mm ahead of the soft-to-hard interface (d = -0.3 mm), the increase in crack growth rate (slope of da/dN vs. ΔK curve) slowed to a steady value (6.44×10^{-5} mm/cycle) as the crack approached the interface, indicating that crack shielding due to suppressed driving force (J-integral) may have affected crack growth in this region. When the crack approached the interface, ΔK was relatively high (about 22 MPa$\sqrt{m}$) and approaching the rapid failure region where only a few scattered data points were collected before final failure. After the crack crossed the interface to the 15-5PH SS side, the crack growth rate increased suddenly to a higher level (1.53×10^{-4} mm/cycle) but was still lower compared with the Paris Law behaviour of the corresponding single-material 15-5PH SS (orange markers). This difference is consistent with the expected effect of the higher compressive residual stress (up to a magnitude of 303 MPa) after the interface on the 15-5PH SS side of the bi-material.

On the bi-material fracture surface shown in Fig. 11(c), the upper 316L SS side exhibited a rough and tortuous crack path, while the 15-5PH SS was smoother and flatter, similar to results obtained from corresponding single material tests. Away from the interface, there are many large defects at the bottom 15-5PH SS layer, also similar to the corresponding single-material (Fig. 6(c)). As discussed previously, it is suspected that at high ΔK (from 22 to 70 MPa$\sqrt{m}$) small process-induced pores were opened and elongated by rapid crack propagation.

Fig. 12 shows SEM images of the bi-material fracture surface within the upper 316L SS, bottom 15-5PH SS, and interfacial regions. Propagation along a more tortuous crack path occurred in 316L SS (Fig. 12(a)), as confirmed by the vertical ridges that follow the large, elongated grains in LPBF 316L SS (area-weighted grain size of 107.9 µm with an aspect ratio of 4.3 ± 3.1 [27]. In 15-5PH SS (Fig. 12(b)), a flat fracture surface can be attributed to the small and short grains (area-weighted grain size of 5.9 µm with an aspect ratio of 2.6 ± 1.2 [27]). The wavy interface appeared to be bonded and defect-free, and crack propagation appeared continuous without any crack bifurcations (Fig. 12(c)). An enlarged view of the interfacial microstructure (Fig. 12(d)) shows that two of the ridge-like features in the 316L SS side (ridges 1 and 2, red arrows) terminated at the interface, however another (ridge 3 indicated by red arrow) deflected as it passed the interface and then stopped after about 20 µm. These ridges behind the crack tip may have had an ongoing shielding effect due to roughness induced crack closure after the crack propagated into the 15-5PH with a smoother resultant fracture surface, but this would have diminished as the crack propagated farther and therefore the crack opening increased.

3.4.2. *Crack propagation from 15-5PH to 316L SS (hard-to-soft)*

In the case of crack propagation from hard 15-5PH to soft 316L SS, the initial crack growth in 15-5PH far from the interface region (Fig. 13(a), green markers) displayed crack growth rate consistent with the Paris Law behaviour of single material 15-5PH SS (orange markers). After the crack grew to a distance of 1.24 mm from the interface, the crack growth rate started to decrease from 9.45×10^{-6} mm/cycle to a local minimum

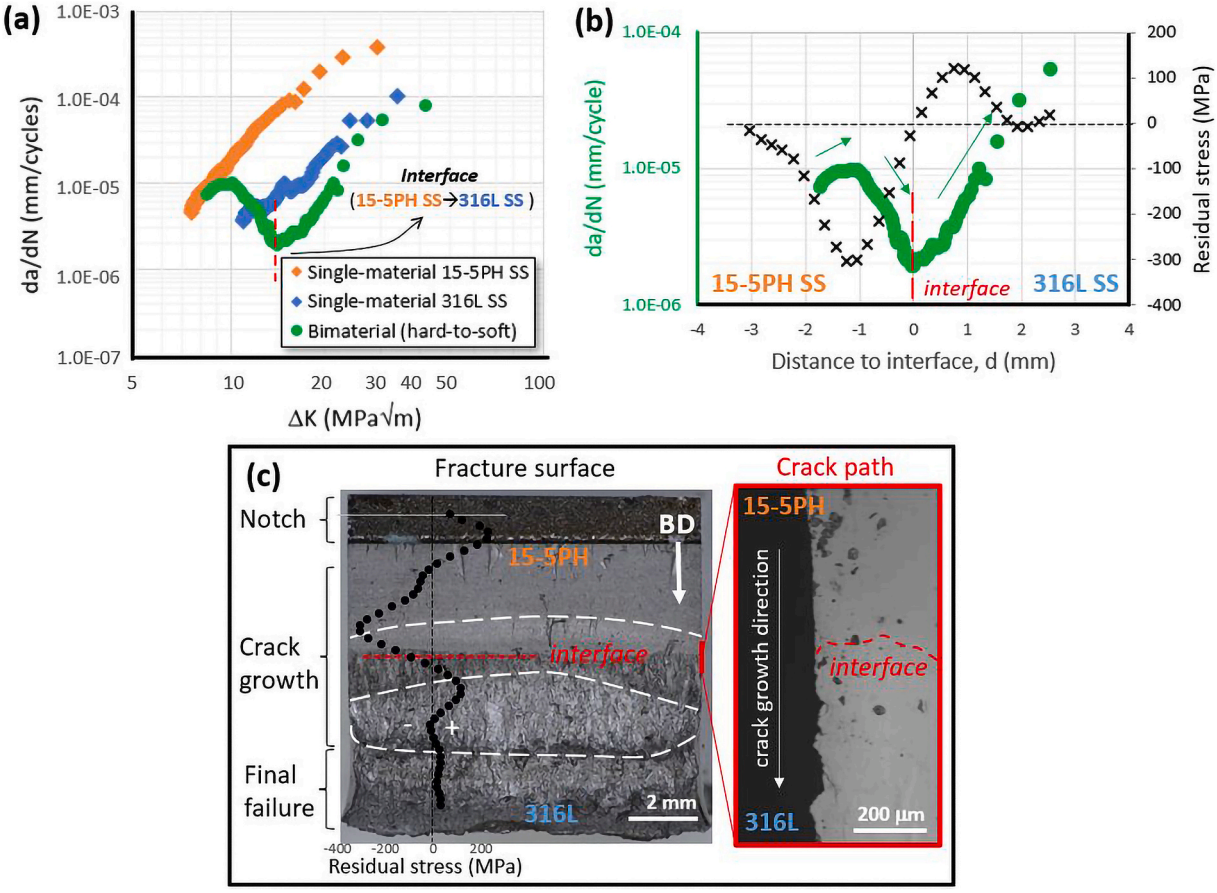

Fig. 13. (a)Crack growth rate, da/dN, versus stress intensity factor range, ΔK, (b)da/dN (green circles) and residual stress (black crosses) from contour cut method versus distance from crack tip to interface, d, and (c) full fracture surface with side views of the crack path (within a region of interest, marked red) for a bi-material with crack growing from 15-5PH SS to 316L SS under constant load. Building direction, BD, and crack growth direction are indicated by arrows.

of 2.10 $\times$ 10^{-6} mm/cycle (a decrease of 77.8 %) when the crack tip reached the hard-to-soft interface. There was no clear increase in propagation rate due to any expected anti-shielding effect as the crack approached the bi-material interface in this hard-to-soft case. The onset of the observed decrease in propagation rate corresponded with the region of highest compressive residual stress (up to 303 MPa in magnitude) on the 15-5PH SS side of the interface (Fig. 13(b)). The effect of compressive residual stress is also apparent from the convex shape of the crack front shown above the interface on the fracture surface in Fig. 13(c), which is expected because the crack-retarding compression would be minimum near the free-surfaces of the specimen edges. After the crack penetrated the 316L SS side, the crack growth accelerated as it reached regions of tensile residual stress (up to 119 MPa in magnitude), but the growth rate remained suppressed relative to the single-material 316L SS until approaching rapid final fracture at high ΔK. In this region (green markers after the interface), the best-fit power law curve for crack growth rate vs. ΔK was da/d$N = 2 \times 10^{-10}\Delta K^{3.5}$. Compared to Equation (2) for single material 316L SS, the value of exponent, which is the slope of the crack growth rate curve on log–log scale, is slightly larger (2.7 for single material 316L SS and 3.5 for 316L SS layer of bi-material), but the intercept is 30 times smaller. Imaging the crack from the side view near the interface region (Fig. 13(c)) shows that the path became more tortuous after passing the interface into the 316L SS side as the crack growth rate increased from a minimum at interface.

Fractographic analysis of the crack propagation through the hard-to-soft interface of the bi-material specimen is displayed in Fig. 14. Above the interface, the fracture surface is flat in the 15-5PH SS layer (Fig. 14(a)) and a tortuous fracture surface with vertical ridges is observed in the 316L layer below the interface (Fig. 14(b)). At the interface region at low magnification (Fig. 14(c)), the interface is wavey (white dashed line). Beneath the interface, vertical ridges were observed in 316L SS layer, as pointed out by a red arrow. Fig. 14(d), a zoomed-in SEM image at interface, shows several vertical micro-cracks (red arrows) beneath the interface, located between primary dendrites within elongated grains of 316L SS. Similar dendritic decohesive crack propagation has been reported previously in 316L SS [14].

3.5. *Fatigue crack propagation of 316L/15-5PH bi-materials at constant ΔK*

As discussed in the section above, in the constant load test with a crack propagating through the soft-to-hard interface, only a few data points within the final failure stage were collected due to the high ΔK level after the crack crossed the interface (Fig. 11). Therefore, the soft-to-hard test was repeated with a constant and relatively low ΔK of 11 MPa$\sqrt{m}$ to avoid increasingly rapid crack growth. The crack growth rate (da/dN) vs. distance from crack tip (d) (purple markers) for this test is plotted in Fig. 15(a), with comparisons to the baseline performance of single material 316L SS (blue markers) and 15-5PH SS (orange markers) under the same level of constant ΔK loading. The interface is marked by a red dashed line. The same da/dN vs. d curve for the bi-material (purple markers) is displayed in Fig. 15(b) with the residual stress distribution from the contour cut method shown (black markers). Initially, the crack in the bi-material specimen grew at a similar, but slightly higher rate, compared with the single-material 316L SS, which is consistent with the higher tensile residual stress ahead of the bi-material interface. When the crack tip was 0.55 mm ahead of the interface, the crack growth rate

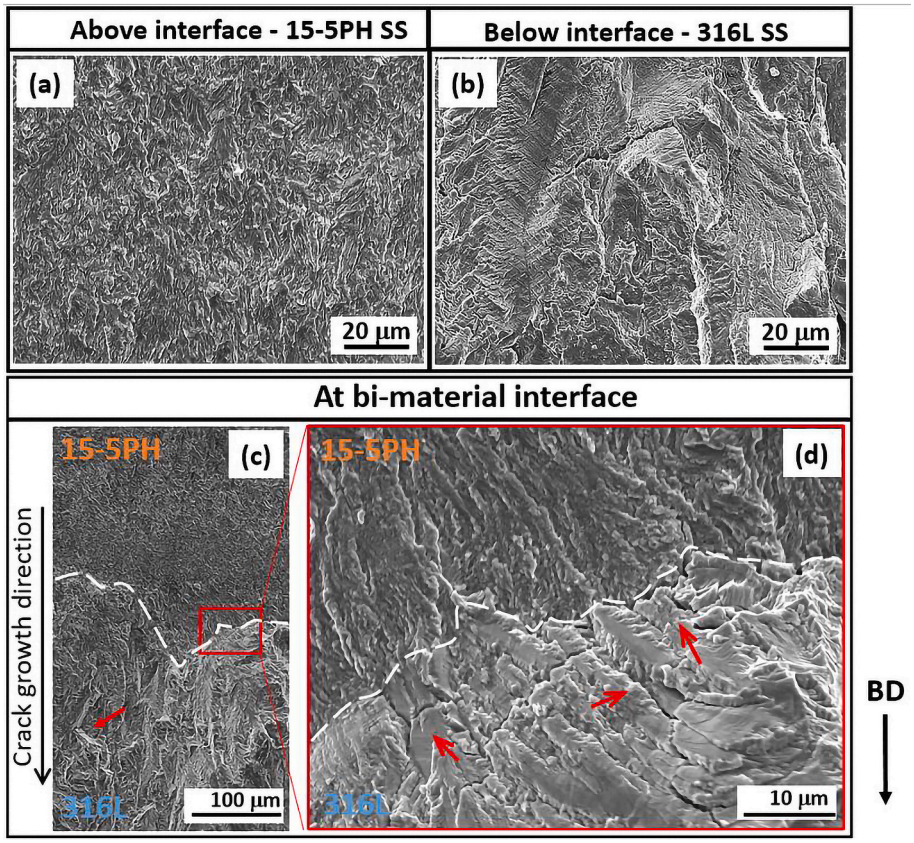

Fig. 14. SEM fractography of a bi-material with a fatigue crack growing from 15-5PH SS to 316L SS at constant load at different locations: (a) 15-5PH SS layer above interface, (b) 316L SS layer below interface, and (c, d) the interfacial region (with 15-5PH above and 316L below) at low and high magnifications. Building direction, BD, and crack growth direction are indicated by arrows.

began to increase up to a maximum of 1.81×10^{-5} mm/cycle at 0.14 mm ahead of the interface (a 262 % increase). The onset of this more rapid propagation correlates with an increase in tensile residual stress to a maximum of 119 MPa. As the crack continued approaching the interface, the growth rate slightly reduced by 6.6 % to 1.69×10^{-5} mm/cycle before reaching the interface, which is similar to the crack growth rate obtained in single material 15-5PH SS under constant ΔK (1.50×10^{-5} mm/cycle). After the crack penetrated the 15-5PH side, the crack growth rate remained relatively stable over a distance of 0.63 mm and at a level consistent with that of single-material 15-5PH SS. However, a sharp reduction in growth rate by 70.7 % was observed when the residual stress dropped into compression and reached a maximum compressive stress of 303 MPa.

Fig. 15(c) displays the entire fracture surface (left) and the crack path at the interface from side view (right). The crack in the top 316L side appears rougher and more tortuous. The crack in the bottom 15-5PH side is flatter with a convex crack front shape before final fracture (white dashed line, Fig. 15(b)), which is indicative of suppression due to compressive residual stress. Compared to the fracture surface on the bottom 15-5PH SS side in the soft-to-hard case under constant load (Fig. 11(c)), there are fewer large defects visible due to the lower constant ΔK of 11 MPa$\sqrt{m}$ (compared to $\Delta K > 25$ MPa$\sqrt{m}$ in 15-5PH regions in Fig. 11). Both samples were manufactured in the same batch, the processing condition are all the same, so the porosity in 15-5PH SS should be similar in all specimens, which again confirms that the larger defects shown in Fig. 11 are not only attributable to the manufacturing process. The SEM images of the fracture surface in the upper 316L SS (Fig. 16(a)), bottom 15-5PH SS (Fig. 16(b)) and interfacial regions (Fig. 16(c)) are shown below and confirm the observations from Fig. 15.

4. Summaries and conclusions

This study investigated the fatigue crack propagation performance and Paris Law behaviour of LPBF fabricated 316L/15-5PH SS bi-material specimens and each corresponding single material. The residual stress distribution along the building direction of bi-material specimens were determined. The shielding and anti-shielding effects on crack propagation due to a plasticity mismatch between the two materials were analysed with FE models. Fatigue tests were carried out with single edge notched bending specimens for LPBF bi-materials, including two constant load tests (one with a crack growing through soft to hard interface; another with a crack growing through hard to soft interface), and one constant-ΔK test for the soft-to-hard case. The main conclusions can be summarized as follows:

- At the same ΔK, the crack growth rate in single-material 15-5PH SS was 4.8 times faster than that in single-material 316L SS. Slower crack propagation was consistent with larger elongated grains and a rougher fracture surface in 316L SS.
- The residual stress distribution measured by hole-drilling and contour methods are consistent with expectations from the temperature gradient mechanism (TGM) and the cool-down phase models. For bi-material specimens built with 15-5PH SS as the bottom layer, a tensile residual stress with a magnitude of up to 119 MPa was measured on the top 316L SS side within 2 mm above interface, while a compressive residual stress with a magnitude of up to 303 MPa was measured on the bottom 15-5PH SS side within 3 mm below the interface.
- The elevated compressive residual stress on the 15-5PH SS side of the bi-materials, balanced by higher tensile residual stress in the 316L SS

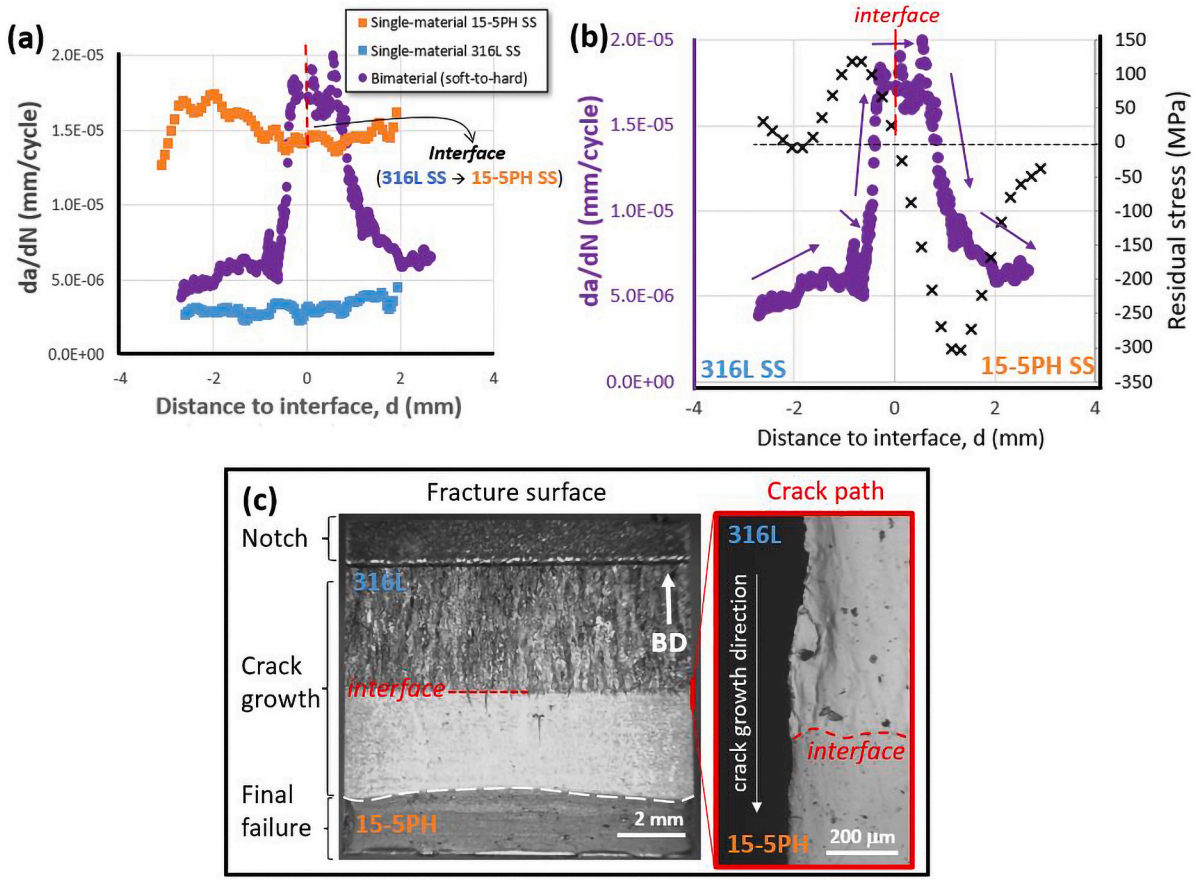

Fig. 15. (a) Crack growth rate, da/dN, versus distance from crack tip to interface position, d, (b) da/dN (purple circles) and residual stress (black crosses) from contour cut method versus d, and (c) full fracture surface with side views of crack path (within region of interest, marked red) in a bi-material with a crack growing from 316L SS to 15-5PH SS under constant ΔK of 11 MPa$\sqrt{\text{m}}$ (decreased load with increased a). Building direction, BD, and crack growth direction are indicated by arrows.

is consistent with the higher CTE of the 316LSS, which would lead to more constraint as it cooled and contracted after fusion.

- A baseline crack growth rate within each region of the bi-material specimens was determined by the Paris Law of the corresponding single material. Local variations from this baseline were likely caused by small shielding/anti-shielding effects (due to mismatch of plasticity) and larger effects of residual stress resulting for multi-material LPBF processing.
- Prediction of the crack shielding effect due to the plasticity mismatch in a 316L/15-5PH bi-material (with yield strength ratio of 1.56) yielded a J-integral decrease of 9.6 % within a distance of 0.03 mm ahead of the soft-to-hard interface (similar to estimated plastic zone size of a crack in the soft material: 0.27 mm), with a small corresponding drop in crack growth rate of 1.3 % based on the Paris law for 316L SS and the value of ΔK under constant load (ΔK = 11 MPa$\sqrt{\text{m}}$) when the crack reached the interface with the hard 15-5PH side.
- The effect of residual stress was more pronounced on crack propagation rate at lower ΔK level of 11 MPa$\sqrt{\text{m}}$. In regions of high residual stress, much larger changes in crack growth rate of up to 77.8 % (the decrease in rate at the location of compressive residual stress of ~ 303 MPa) were observed.

Based on these findings, a strategy for improved damage tolerance of LPBF materials can be suggested using multi-material processing capabilities. The compressive residual stress resulting at locations where 15-5PH SS layers are processed below 316L SS can be used as a potent suppressor of crack propagation. These layers can be positioned surrounding locations of expected crack initiation, such as surfaces or stress-concentrating features. However, the higher rate of crack propagation through 15-5PH SS in the absence of residual stress means that the thickness of such layers should be minimised within 316L SS parts. The potential effects of bi-material interfaces on strength, crack initiation, and therefore total lifetime should also be considered and requires further investigation.

CRediT authorship contribution statement

Anqi Liang: Writing – original draft, Visualization, Validation, Project administration, Methodology, Investigation, Formal analysis, Data curation, Conceptualization. **Songsong Lu:** Writing – review & editing, Visualization, Methodology, Investigation, Formal analysis, Data curation, Conceptualization. **Mitchell Leering:** Writing – review & editing, Visualization, Methodology, Investigation, Formal analysis, Data curation, Conceptualization. **Bilal Ahmed:** Writing – review & editing, Visualization, Methodology, Investigation, Formal analysis, Data curation, Conceptualization. **Michael E. Fitzpatrick:** Supervision, Resources, Methodology. **Philippa A.S. Reed:** Writing – review & editing, Supervision, Resources, Methodology, Conceptualization. **Tomas Polcar:** Supervision, Resources. **Andrew R. Hamilton:** Writing – review & editing, Supervision, Resources, Project administration, Methodology, Conceptualization.

Declaration of competing interest

The authors declare that they have no known competing financial

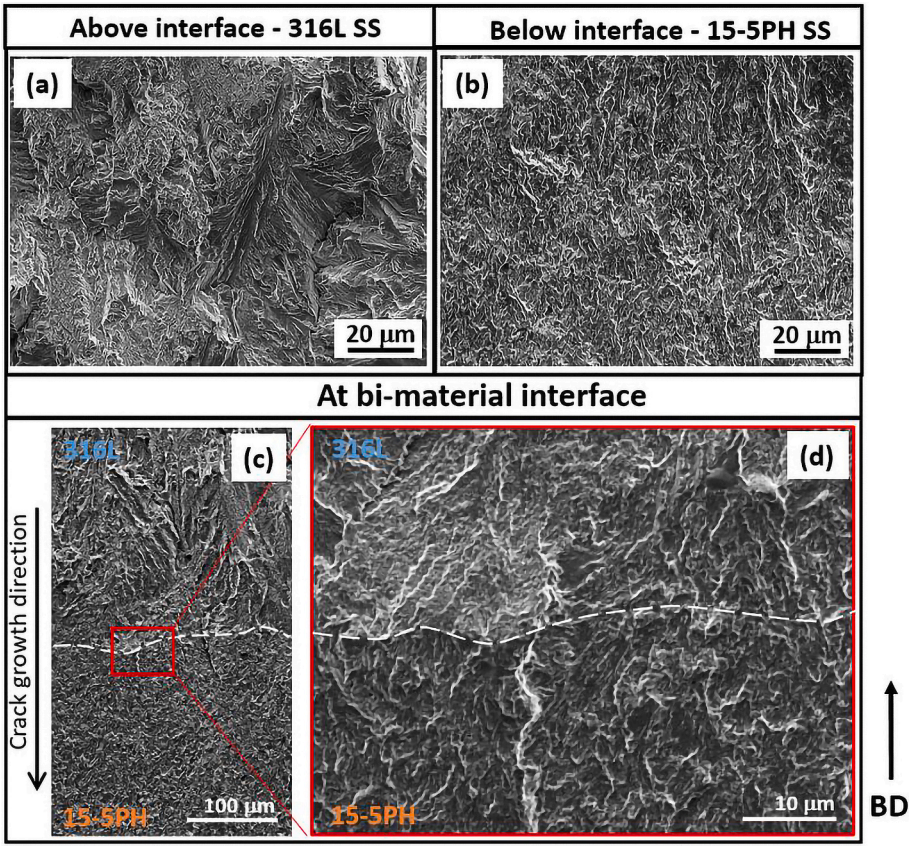

Fig. 16. SEM fractography of a bi-material component with a fatigue crack growing from 316L SS to 15-5PH SS at constant ΔK (11 MPa$\sqrt{m}$) at different locations: (a) 316L SS layer above interface, (b) 15-5PH SS layer below interface, and (c, d) the interfacial region (with 316L above and 15-5PH below) at low and high magnifications. Building direction, BD, and crack growth direction are indicated by arrows.

interests or personal relationships that could have appeared to influence the work reported in this paper.

Acknowledgements

Anqi Liang was supported by a partial scholarship from the Faculty of Engineering and Physical Sciences at the University of Southampton.

Data availability

Data supporting this study are openly available from the University of Southampton repository at https://doi.org/10.5258/SOTON/D3593.

References

[1] Hinojos A, et al. Joining of Inconel 718 and 316 Stainless Steel using electron beam melting additive manufacturing technology. Mater Des 2016;94:17–27.
[2] Griffis J, Shahed K, Meinert K, Yilmaz B, Lear M, Manogharan G. Multi-material laser powder bed fusion: effects of build orientation on defects, material structure and mechanical properties. npj Adv Manuf 2025;2(1):5.
[3] Chen J, Yang Y, Song C, Wang D, Wu S, Zhang M. Influence mechanism of process parameters on the interfacial characterization of selective laser melting 316L/CuSn10. Mater Sci Eng A 2020;792:139316.
[4] Shakerin S, Hadadzadeh A, Amirkhiz BS, Shamsdini S, Li J, Mohammadi M. Additive manufacturing of maraging steel-H13 bimetals using laser powder bed fusion technique. Addit Manuf 2019;29:100797.
[5] Inoue J, Nambu S, Ishimoto Y, Koseki T. Fracture elongation of brittle/ductile multilayered steel composites with a strong interface. Scr Mater 2008;59(10):1055–8.
[6] Bandyopadhyay A, Heer B. Additive manufacturing of multi-material structures. Mater Sci Eng R Rep 2018;129:1–16.
[7] Shrestha R, Shamsaei N, Seifi M, Phan N. An investigation into specimen property to part performance relationships for laser beam powder bed fusion additive manufacturing. Addit Manuf 2019;29.
[8] Gerard D, Koss D. The influence of porosity on short fatigue crack growth at large strain amplitudes. Int J Fatigue 1991;13(4):345–52.
[9] Rezanezhad M, Lajevardi SA, Karimpouli S. Effects of pore (s)-crack locations and arrangements on crack growth modeling in porous media. Theor Appl Fract Mech 2020;107:102529.
[10] Riemer A, Leuders S, Thöne M, Richard H, Tröster T, Niendorf T. On the fatigue crack growth behavior in 316L stainless steel manufactured by selective laser melting. Eng Fract Mech 2014;120:15–25.
[11] Kolednik O. The yield stress gradient effect in inhomogeneous materials. Int J Solids Struct 2000;37(5):781–808.
[12] Song XX, Shang YB, Shi HJ, Niu LS, Wang ZX. Plastic mismatch effect on plasticity induced crack closure: fatigue crack propagation perpendicularly across a plastically mismatched interface. Fatigue Fract Eng Mater Struct 2019;42(3):597–611.
[13] Jiang F, Deng Z, Zhao K, Sun J. Fatigue crack propagation normal to a plasticity mismatched bimaterial interface. Mater Sci Eng A 2003;356(1–2):258–66.
[14] Duval-Chaneac M-S, et al. Fatigue crack growth in IN718/316L multi-materials layered structures fabricated by laser powder bed fusion. Int J Fatigue 2021;152:106454.
[15] Kümmel F, Höppel HW, Göken M. Layer architecture and fatigue life of ultrafine-grained laminated metal composites consisting of different aluminum alloys. Mater Sci Eng A 2017;702:406–13.
[16] Pribe JD, Siegmund T, Kruzic JJ. The roles of yield strength mismatch, interface strength, and plastic strain gradients in fatigue crack growth across interfaces. Eng Fract Mech 2020;235:107072.
[17] Pippan R, Flechsig K, Riemelmoser F. Fatigue crack propagation behavior in the vicinity of an interface between materials with different yield stresses. Mater Sci Eng A 2000;283(1–2):225–33.
[18] Kümmel F, Diepold B, Prakash A, Höppel HW, Göken M. Enhanced monotonic and cyclic mechanical properties of ultrafine-grained laminated metal composites with strong and stiff interlayers. Int J Fatigue 2018;116:379–87.
[19] Demir AG, Previtali B. Multi-material selective laser melting of Fe/Al-12Si components. Manuf Lett 2017;11:8–11.
[20] Santos LM, Ferreira JA, Borrego LP, Costa JD, Capela C, de Jesus J. Fatigue crack propagation along interfaces of selective laser melting steel hybrid parts. Fatigue Fract Eng Mater Struct 2019;42(11):2431–40.
[21] Gomes DDA, Castro JA, Xavier CR, Lima CAC. Analysis of residual stress by the hole-drilling method and hardness in dissimilar joints of austenitic stainless steel AISI 316L and Inconel 718 alloy by autogenous GTAW process. Mater Res 2019;22.

[22] Li W, et al. Fabrication and characterization of a functionally graded material from Ti-6Al-4V to SS316 by laser metal deposition. Addit Manuf 2017;14:95–104.
[23] Kruth J-P, Deckers J, Yasa E, Wauthlé R. Assessing and comparing influencing factors of residual stresses in selective laser melting using a novel analysis method. Proc Inst Mech Eng B J Eng Manuf 2012;226(6):980–91.
[24] Mukherjee T, Zhang W, DebRoy T. An improved prediction of residual stresses and distortion in additive manufacturing. Comput Mater Sci 2017;126:360–72.
[25] Mercelis P, Kruth JP. Residual stresses in selective laser sintering and selective laser melting. Rapid Prototyping J 2006;1.
[26] Bai Y, Zhang J, Zhao C, Li C, Wang H. Dual interfacial characterization and property in multi-material selective laser melting of 316L stainless steel and C52400 copper alloy. Mater Charact 2020;167:110489.
[27] Liang A, Sahu S, Zhao X, Polcar T, Hamilton AR. Interfacial characteristics of austenitic 316 L and martensitic 15–5PH stainless steels joined by laser powder bed fusion. Mater Charact 2023;198:112719.
[28] ISO 12108:2018 Metallic materials — Fatigue testing — Fatigue crack growth method; 2018.
[29] Glinka G. Development of weight functions and computer integration procedures for calculating stress intensity factors around cracks subjected to complex stress fields. Stress and Fatigue-Fracture Design, Petersburg Ontario, Canada, Progress Report 1996;1(1):1.
[30] ASTM International, E399-22, Standard Test Method for Linear-Elastic Plane-Strain Fracture Toughness of Metallic Materials; 2022.
[31] Weiss K, Hetzler S, Kvackaj T, Bidulsky R, Grande MA, Manfredi D. Cryogenic material properties of additive manufactured 316L stainless steel. In: IOP Conference Series: Materials Science and Engineering, vol. 1241, no. 1. IOP Publishing; 2022, 012047.
[32] Ramadas H, Nath AK, Sarkar S, Ganesh P, Kaul R, Majumdar JD. Fatigue crack growth rate and fracture toughness evaluation of 15-5 precipitation hardening stainless steel fabricated by laser powder bed fusion process. Mater Sci Eng A 2022; 861:144356.
[33] Kolednik O, Predan J, Shan G, Simha N, Fischer FD. On the fracture behavior of inhomogeneous materials—a case study for elastically inhomogeneous bimaterials. Int J Solids Struct 2005;42(2):605–20.
[34] Lu S, Laborda A, Cook R, Zhang Y, Verbickas R, Reed P. A numerical study of crack shielding/anti-shielding in layered architectures. Int J Fatigue 2019;124:503–19.
[35] ASTM E837 Standard Test Method for Determining Residual Stresses by the Hole-Drilling Strain-gauge Method; 2020.
[36] Shiomi M, Osakada K, Nakamura K, Yamashita T, Abe F. Residual stress within metallic model made by selective laser melting process. CIRP Ann 2004;53(1): 195–8.
[37] Simson T, Emmel A, Dwars A, Böhm J. Residual stress measurements on AISI 316L samples manufactured by selective laser melting. Addit Manuf 2017;17:183–9.
[38] Williams RJ, Vecchiato F, Kelleher J, Wenman MR, Hooper PA, Davies CM. Effects of heat treatment on residual stresses in the laser powder bed fusion of 316L stainless steel: finite element predictions and neutron diffraction measurements. J Manuf Process 2020;57:641–53.
[39] Zhang W, Jiang W, Zhao X, Tu S-T. Fatigue life of a dissimilar welded joint considering the weld residual stress: experimental and finite element simulation. Int J Fatigue 2018;109:182–90.
[40] Fergani O, Bratli Wold A, Berto F, Brotan V, Bambach M. Study of the effect of heat treatment on fatigue crack growth behaviour of 316L stainless steel produced by selective laser melting. Fatigue Fract Eng Mater Struct 2018;41(5):1102–19.
[41] Ritchie RO. Mechanisms of fatigue-crack propagation in ductile and brittle solids. Int J Fract 1999;100(1):55–83.
[42] Bantounas I, Lindley TC, Rugg D, Dye D. Effect of microtexture on fatigue cracking in Ti–6Al–4V. Acta Mater 2007;55(16):5655–65.
[43] Sugimura Y, Lim P, Shih C, Suresh S. Fracture normal to a bimaterial interface: effects of plasticity on crack-tip shielding and amplification. Acta Metall Mater 1995;43(3):1157–69.